AIAA JOURNAL
Vol. 43, No. 5, May 2005

Analysis and Prediction of Thin-Airfoil Stall Phenomena with Hybrid Turbulence Methodology

Soshi Kawai*
University of Tokyo, Tokyo 113-8656, Japan
and
Kozo Fujii†
Japan Aerospace Exploration Agency, Kanagawa 229-8510, Japan

Analysis and prediction of thin-airfoil stall phenomena of a NACA 64A006 airfoil are numerically investigated using large-eddy simulation (LES)/Reynolds-averaged Navier–Stokes (RANS) hybrid methodology with a high-order compact differencing scheme. Subsonic flow of $M_\infty = 0.17$ with the high Reynolds number of $Re = 5.8 \times 10^6$ is considered, and the angle of attack is varied from 4.0 to 11.0 deg. The results illustrate the possibility of the present LES/RANS hybrid methodology for the prediction of the massively separated high Reynolds number flows with laminar separation and turbulent reattachment within more practical computational cost than that of a pure LES approach. Thin-airfoil stalling aerodynamic characteristics are successfully predicted using the LES/RANS hybrid methodology with a high-order compact difference scheme that is less costly than pure LES approaches. For the prediction of thin-airfoil stall phenomena, it is necessary to resolve properly the laminar small bubble near the leading edge at relatively low angles of attack and the growth of the bubble where suction pressure peak collapses with increasing angles of attack. From the instantaneous and time-averaged flows, it is confirmed that the laminar small bubble near the leading edge is a phenomenon that appears when the unsteady small vortices shedding from the leading edge are averaged for a certain length of time. High-order compact differencing scheme provides extremely high-fidelity results for the complicated and separated flowfields associated with a NACA 64A006 airfoil near stall, even under the reasonable number of grid points. Thin-airfoil stall characteristics are well predicted with the numerical transition method implemented in the original Baldwin and Lomax turbulence model that detects the transition point automatically from the computation. The LES/RANS hybrid methodology with the simple transition method is considered to be an effective prediction tool for flows where the RANS can predict the transition reasonably well.

Nomenclature

a	=	sonic speed
C_K	=	Yoshizawa model coefficient
C_L	=	lift coefficient, lift/$(q_\infty S_{\text{ref}})$
C_p	=	local pressure coefficient, $(p - p_\infty)/(q_\infty S_{\text{ref}})$
C_S	=	Smagorinsky model coefficient
c	=	chord length of the profile
d_{blend}	=	distance from wall to blending position
d_{wall}	=	distance from wall
M	=	local Mach number
Pr_t	=	turbulent Prandtl number
p	=	local static pressure
p_t	=	local total pressure
q	=	dynamic pressure
q_j^{SGS}	=	subgrid-scale heat flux vector
Re	=	Reynolds number
S_{ij}	=	strain rate tensor
S_{ref}	=	reference area
T	=	temperature
u	=	local velocity
x, y, z	=	Cartesian coordinates
x_j	=	coordinate vector
α	=	angle of attack
α_f	=	filter strength coefficient
γ	=	ratio of specific heats
Δ_{filter}	=	filter length scale
Δt	=	integration time
$\Delta x, \Delta y, \Delta z$	=	step size of the grid in x, y, and z directions
δ_{ij}	=	Kronecker delta
μ_t	=	turbulent eddy viscosity
μ_t^{SGS}	=	subgrid-scale turbulent eddy viscosity
ν	=	kinematic eddy viscosity
ν_t^{SGS}	=	subgrid-scale kinematic eddy viscosity
ρ	=	density
τ_{ij}^{SGS}	=	subgrid-scale stress tensor

Subscripts

∞	=	freestream quantity
BL	=	quantity at outer edge of boundary layer

Superscripts

$-$	=	spatially filtered quantity
$\sim$	=	Favre-filtered quantity
$+$	=	wall unit quantity
$*$	=	dimensional quantity

Received 20 June 2004; presented as Paper 2004-2714 at the AIAA 34th Fluid Dynamics Conference, Portland, OR, 28 June–1 July 2004; revision received 4 November 2004; accepted for publication 23 November 2004.

*Research Fellow of the Japan Society for the Promotion of Science, Department of Aeronautics and Astronautics, 7-3-1 Hongo, Bunkyo-ku; kawai@flab.eng.isas.jaxa.jp. Member AIAA.

†Professor, Department of Space Transportation Engineering, Institute of Space and Astronautical Science, 3-1-1, Yoshinodai, Sagamihara; fujii@flab.eng.isas.jaxa.jp. Fellow AIAA.

I. Introduction

PRECISE estimation of maximum lift and stall angle of a wing is an important issue for the aerodynamic design of aircraft. Whereas the conventional computational fluid dynamics (CFD) technology has enabled precise numerical analysis of attached flows at relatively low angles of attack, it is still difficult to simulate

massively separated unsteady turbulent flows at high angles of attack near stall. Therefore, it is important and necessary to develop a CFD technology for the prediction of such unsteady flows at high Reynolds numbers within a reasonable computational cost.

In the workshop sponsored by the National Aerospace Laboratory of Japan in 2000, CFD predictions of the stall characteristics of three types of wing sections were discussed: NACA 63-018, NACA 63-012, and NACA 64A006. The stall characteristics of the NACA 63-018 and the NACA 63-012 are classified into trailing-edge stall and leading-edge stall, respectively, and are well predicted by the conventional Reynolds-averaged Navier–Stokes (RANS) computations.[1] However, prediction of stall characteristics of the NACA 64A006 airfoil at high Reynolds numbers was not successful. This airfoil has thin-airfoil stall characteristics, where the laminar flow separation occurs at the leading edge and the transition causes the turbulent reattachment. The reattachment point gradually moves rearward with increasing angles of attack. Flows over a thin airfoil at the angle of attack beyond 5.0 deg include small vortices shedding from the leading edge, which produces strong unsteadiness in the flow. This is the main reason that RANS simulations in which we deal with time-averaged quantities using turbulence models do not give satisfactory results.

The limitation of RANS simulations led to an interest in methods such as large-eddy simulation (LES) that may improve the prediction accuracy of such flows. Thanks to the rapid progress of computer capability in recent years, LES has been applied to the flows of some airfoils near stall at high Reynolds numbers.[2–4] It is suggested in Ref. 2 that LES can successfully resolve the turbulent transition directly and predict the flow behavior, including separation and reattachment, if the mesh is adequately fine near the walls and resolves near-wall turbulent structures, whereas the results with coarse mesh resolution are generally disappointing. The mesh resolution required for the simulations using LES becomes enormous when LES is applied to the wall-bounded flows at high Reynolds numbers. In particular, an extremely fine resolution is needed for resolving turbulent transition. In addition, in order to maintain temporal accuracy inside a boundary layer, computational time step size is limited. In fact, in the best prediction by LES of Mary and Sagaut,[3] the spanwise extent of the computational domain is limited to 1.2% of the chord length, and the three-dimensional computational domain is only located near the solid surface. Given the feasibility of LES under the current computer environment, it still remains difficult to apply LES to complex flows at high Reynolds numbers as seen in many engineering problems.

To overcome these difficulties, an LES/RANS hybrid methodology was proposed in recent years. The LES/RANS hybrid approach applies RANS computation based on Favre-averaged Navier–Stokes equations to the regions near solid surfaces, whereas LES computation based on Favre-filtered Navier–Stokes equations is applied to the other region that may include massively separated flows. The hybrid methodology is considered to require a lower computational cost than LES because it can alleviate immense grid requirements and the severe time-step limitation associated with the small-eddy motions that need to be resolved in the wall-bounded regions. LES/RANS hybrid methodology was successfully applied to a supersonic turbulent mixing flow[5] and supersonic axisymmetric base flow.[6] Both of the cases have shown the reliability and capability of the hybrid method when the separation line is fixed at the edge of the splitter plate and the base edge. The reliability of the hybrid methodology for flows with massive separation, transition, and reattachment is not yet fully identified.

Another approach to capture massively separated high Reynolds number flows is detached-eddy simulation (DES).[7] DES is a simple modification of the Spalart–Allmaras (SA) turbulence model[8] and switches from RANS (SA) to LES-like simulation away from the solid surface. DES has been applied to a flow past a circular cylinder[9] with laminar and turbulent separation where the separation line was not fixed. Major features of the separated flow such as drag, shedding frequency, and pressure were reasonably well predicted with DES but not with unsteady RANS, whereas the prediction accuracy of the length of the recirculation bubble was poor. The partial success described in Ref. 9 may be considered to prove the validity and capability of DES to flows with massive separation and transition. However, this case did not have turbulent reattachment.

In the present study, the LES/RANS hybrid methodology is applied to subsonic flows at high Reynolds numbers around a NACA 64A006 airfoil at various angles of attack. The purpose of the present paper is to achieve a highly-fidelity prediction of the maximum lift and stall angle of the thin-airfoil stall characteristic by CFD within a practical computational cost and to identify the reliability and capability of the LES/RANS hybrid methodology for flows with separation, transition, and turbulent reattachment. Spatial derivatives of governing equations are evaluated by the sixth-order compact difference scheme proposed by Lele.[10] The compact difference scheme achieves the spectrallike resolution with minimum dispersive and dissipative numerical errors. The computational conditions are set to be the same as those of the experiments of McCullough and Gault.[11,12] The computational results are compared with those by the conventional upwind scheme and the experiment. The mechanism of the bubble appearing at the leading edge is discussed. The influence of the different schemes under the current mesh resolution and the effect of transition methods are both investigated.

II. Mathematical Model

A. Governing Equations

Both Favre-filtered Navier–Stokes equations and Favre-averaged Navier–Stokes equations are derived from the compressible form of Navier–Stokes equations. The details of this derivation are provided in Ref. 6. Both the Favre-filtered and the Favre-averaged Navier–Stokes equations for an ideal gas are nondimensionalized by the density and the speed of sound of the freestream and the characteristic length c and are transformed to the generalized curvilinear coordinate system. The Favre-averaged Navier–Stokes equations with modeled correlation terms are used for RANS formulation. The Favre-filtered Navier–Stokes equations with modeled subgrid-scale (SGS) terms are used for LES formulation. Because of the similar form of the RANS and LES formulations, both formulation sets are solved with a single computational method. Sutherland's law is used to compute molecular dynamic viscosity. The Prandtl number and specific heat ratio are fixed to 0.72 and 1.4, respectively.

B. SGS Modelings

SGS terms in the LES formulation cannot be directly computed. Therefore, SGS models have to be introduced to close the system of Favre-filtered equations.

Various models for the SGS stress tensor τ_{ij}^{SGS} have been proposed to solve incompressible filtered Navier–Stokes equations. The SGS modeling used in the present study for compressive flow analyses is based on the incompressible Smagorinsky model.[13] Additional terms to account for compressibility are modeled based on the work of Yoshizawa,[14] Moin et al.,[15] Vreman,[16] and Vreman et al.[17,18]

The SGS stress tensor τ_{ij}^{SGS} is modeled using the Smagorinsky eddy viscosity formulation because of its robustness and low computational cost,

$$\bar{\rho}\tau_{ij}^{\mathrm{SGS}} - \tfrac{1}{3}\delta_{ij}\bar{\rho}\tau_{kk}^{\mathrm{SGS}} = -2\bar{\rho}\nu_t^{\mathrm{SGS}}\tilde{S}_{ij} = -2\bar{\rho}Cs^2\Delta_{\mathrm{filter}}^2|\tilde{S}|\tilde{S}_{ij} \tag{1}$$

The SGS eddy viscosity is analogous to the eddy viscosity used in RANS turbulence models and is written as

$$\mu_t^{\mathrm{SGS}} = \bar{\rho}Cs^2\Delta_{\mathrm{filter}}^2|\tilde{S}| \tag{2}$$

The Δ_{filter} in Eq. (1) is chosen to be a characteristic length of computational grid. This length varies over the grid because of its nonuniform nature. The filter length scaled at each grid point is evaluated by Deardorff's determination as follows:

$$\Delta_{\mathrm{filter}} = (\Delta x\Delta y\Delta z)^{-\frac{1}{3}} \tag{3}$$

$|\tilde{S}|$ in Eq. (1) is defined as

$$|\tilde{S}| = \sqrt{2\tilde{S}_{ij}\tilde{S}_{ij}} \tag{4}$$

As the isotropic part of the SGS stress tensor, $\bar{\rho}\tau_{kk}^{\mathrm{SGS}}$ cannot be computed directly. It must be modeled. In this study, the Yoshizawa model[14] is applied for the computation of the isotropic part of the SGS stress tensor,

$$\bar{\rho}\tau_{kk}^{\mathrm{SGS}} = 2\bar{\rho}C_k\Delta_{\mathrm{filter}}^2|\tilde{S}|^2 \tag{5}$$

The eddy diffusivity model is applied to the SGS heat flux term,

$$q_j^{\mathrm{SGS}} = -\frac{\partial}{\partial x_j}\left[\frac{\bar{\rho}\nu_t^{\mathrm{SGS}}}{(\gamma-1)Pr_tM^2}\frac{\partial\tilde{T}}{\partial x_j}\right] \tag{6}$$

with the turbulent Prandtl number Pr_t fixed to 0.9.

It was shown in Ref. 16 that the other SGS terms as shown in Ref. 6 have a negligibly small value compared to the preceding SGS terms. In this study, those terms are neglected based on the work of Moin et al.[15] and Vreman.[16]

C. LES/RANS Hybrid Methodology

In the LES/RANS hybrid methodology, the RANS formulation is applied to the regions near the solid surface inside the boundary layer, whereas the LES formulation is applied to massively separated flow regions. The motivation of the hybrid method is to alleviate the immense grid requirements and resultant severe time-step limitation associated with the small-eddy motions that need to be resolved in the wall-bounded regions.

In our LES/RANS hybrid method, the Baldwin and Lomax algebraic model[19] is used for the RANS computation and the compressible form of the Smagorinsky model[13] is used for the LES computation to achieve both robustness and low computational cost. These properties often become significant advantages when the LES/RANS hybrid method is applied to engineering problems.

Near the interface of the RANS and LES regions, the RANS (correlation terms being modeled) and LES (SGS terms being modeled) formulation sets are blended by the following method:

$$[\mathrm{LES/RANS\ hybrid}] = \Gamma(\eta)[\mathrm{LES}] + [1-\Gamma(\eta)][\mathrm{RANS}] \tag{7}$$

The blending function $\Gamma(\eta)$ used in the present study is

$$\Gamma(\eta) = \frac{1}{2} + \tanh\left[\frac{C_1(0.2\eta - C_2)}{0.2(1-2C_2)\eta + C_2}\right] \Big/ 2\tanh(C_1) \tag{8}$$

where $\eta = d_{\mathrm{wall}}/d_{\mathrm{blend}}$ (d_{wall} and d_{blend} being distance from the wall and distance from the wall to blending position, respectively), $C_1 = 4$, and $C_2 = 0.2$. A similar expression is used for the weighting function of the inner and outer regions in the boundary layer.[20] The present blending function is continuous from the RANS region through the LES region. The blending function is zero at $\eta = 0$ and $\Gamma(\eta) = 0.5$ at $\eta = 1.0$. The parameter C_1 controls the blending width of the LES and RANS region where the function changes from 0 to 1 as shown in Fig. 1. Transition from the RANS near the solid surface to the LES is designed around the location specified from the surface of the wall d_{blend} with Eq. (8). To apply the RANS turbulence model to the boundary layer, the d_{blend} is specified using the boundary-layer thickness of the result from the a priori RANS simulation. The blending function $\Gamma(\eta)$ is 0.5 at the outer edge of the boundary layer where the effect of LES and RANS is halved. The value rapidly increases to 1.0 away from the boundary-layer edge. The blending point that appears to take place within the boundary layer is not appropriate because the LES region appears near the solid surface and an immense grid point is required to resolve the near-wall turbulence. Increasing the required grid point inside the boundary layer results in a loss of the advantage of the present hybrid method. Distribution of the blending function $\Gamma(\eta)$ around the leading edge of the NACA 64A006 airfoil is shown in Fig. 2.

Time-averaged quantities in the RANS formulation are theoretically different from spatially filtered quantities in LES formulation.

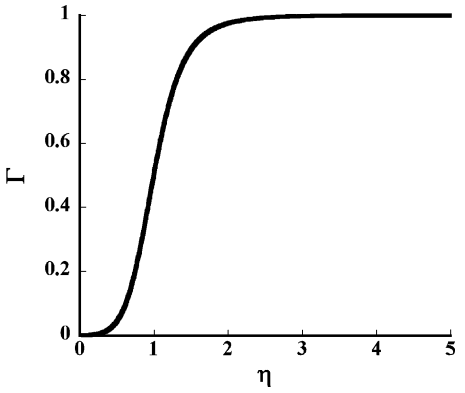

Fig. 1 Behavior of blending function $\Gamma(\eta)$.

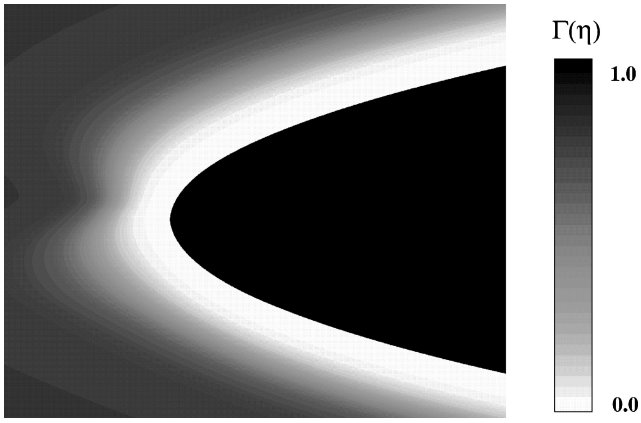

Fig. 2 Distribution of blending function $\Gamma(\eta)$ around the leading edge of a NACA 64A006 airfoil.

However, because of the similar form of the RANS and LES formulations, both formulation sets can be solved continuously from the RANS region through the LES region with a single computational method. We expect the RANS-to-LES region to switch from fully modeled stresses given by the turbulence model to resolved stresses that appear when an unsteady flow is averaged, as discussed in Ref. 21. As a procedure of the present hybrid simulation, the Baldwin–Lomax (BL) turbulence model and the compressible form of the Smagorinsky model are computed to close the RANS and LES formulations at each time step. Then, both formulation sets are solved continuously from the RANS regions through the LES in time-dependent form.

D. Model Constants

The Smagorinsky constant is not a universal constant in the LES of various types of turbulent flows. Therefore, the constants for the SGS models are chosen based on previous studies. Vreman et al.[18] derived the relation between C_S and C_K. This inequality expresses a necessary condition for realizability of SGS stress tensor:

$$C_K \geq \left(\sqrt{3}/2\right)C_S^2 \tag{9}$$

Erlebacher et al.[22] derived the model constants based on the results of their direct numerical simulation and concluded that $C_S^2 = 0.012$. Yoshizawa[14] proposed that $C_S = 0.16$ and $C_K = 0.0886$ from the two-scale direct interaction approximation. Rogallo and Moin[23] suggested the range of $0.10 \leq Cs \leq 0.24$. Based on these previous studies, $Cs = 0.12$ and $C_K = 0.00498$ are chosen for the present thin-airfoil stall analyses. These constants clearly satisfy inequality (9) and the range of $0.10 \leq C_S \leq 0.24$.

E. Numerical Scheme

A high-order central difference discretization with spectrallike resolution that minimizes dispersive and dissipative numerical errors is preferable for LES. Because of their spectrallike resolution,

Table 1 Description of computed cases

Case	Numerical method	Numerical scheme	Transition model
Cmpt-0.2%	LES/RANS hybrid method	Sixth-order compact scheme	Fixed at 0.2% chord length
Cmpt-BL	LES/RANS hybrid method	Sixth-order compact scheme	Baldwin and Lomax's treatment
Upwind-0.2%	LES/RANS hybrid method	SHUS + third-order MUSCL	Fixed at 0.2% chord length

high-order compact difference schemes are an attractive choice for reducing dispersion, anisotropy, and dissipation errors associated with the spatial discretization. Recently, the compact difference scheme was applied to several engineering problems such as vortical flow over a delta wing,[24] a double-delta wing,[25] and the unsteady flow over a wing section near stall condition.[26] The advantage of the compact difference scheme was shown for the vortical flows compared with the conventional second- or third-order scheme.

In this study, the equations are solved in the generalized curvilinear coordinates, where the spatial derivatives for convective terms, viscous terms, metrics, and Jacobian are evaluated by the following sixth-order compact difference scheme.[10] For any scalar quantity f, the finite difference approximation to the first spatial derivatives at node i f'_i are obtained by the following formula:

$$\alpha_{\text{cmpt}} f'_{i-1} + f'_i + \alpha_{\text{cmpt}} f'_{i+1} = a\frac{f_{i+1} - f_{i-1}}{2h} + b\frac{f_{i+2} - f_{i-2}}{4h} \tag{10}$$

where $\alpha_{\text{cmpt}} = 1/3$, $a = 14/9$, and $b = 1/9$ for the sixth-order scheme and where h shows discretization step size. Because the preceding scheme has five stencils in the right-hand side and three stencils in the left-hand side, the fourth and sixth-order explicit one-side biased finite difference schemes are used for the evaluation of the derivatives at the boundary and the neighboring points,[27] respectively.

For the compact difference scheme, a filtering procedure is needed to suppress the numerical instabilities. The following sixth-order filtering scheme[28] is used,

$$\alpha_f \hat{f}_{i-1} + \hat{f}_i + \alpha_f \hat{f}_{i+1} = \sum_{n=0}^{N} \frac{a_n}{2}(f_{i+n} + f_{i-n}) \tag{11}$$

where $\boldsymbol{f}$ is the solution vector and $\hat{f}$ is the filtered quantity. In Eq. (11), the sixth-order ($N = 6$) filter is obtained with $a_0 = (11/16) + (5\alpha_f/8)$, $a_1 = (15/32) + (17\alpha_f/16)$, $a_2 = (-3/16) + (3\alpha_f/8)$, $a_3 = (1/32) + (\alpha_f/16)$, $a_4 = 0$, and $a_5 = 0$. Additionally, the fourth-order filter is adapted at the second point of the boundary for stability. The α_f is a free parameter satisfying the inequality $-0.5 < \alpha_f \leq 0.5$. In this range, a higher value of α_f corresponds to a less dissipative filter. The α_f is set as 0.4 in this study.

Computations are also carried out with the simple high-resolution upwind scheme[29] (SHUS), which belongs to a family of conventional advection upstream splitting method[30] type schemes. When the SHUS scheme is used, physical properties at the interface are evaluated by MUSCL interpolation[31] based on the primitive variables to maintain third-order space accuracy. The viscous terms are evaluated by second-order central differencing scheme.

The lower–upper symmetric Gauss–Seidel factorization implicit algorithm[32] is used for the time integration. However, because the flowfield considered in this study is essentially unsteady, multiple sub-iterations are adopted, and the error due to the linearization is eliminated. In this study, second-order temporal accuracy of the scheme is guaranteed by three-level backward differencing formula.

F. Boundary Conditions

The inflow boundary condition is applied to all of the curved boundaries of the C mesh. In this study, three-dimensional turbulent structures developed naturally without any external perturbations. A characteristic boundary condition is applied to the outflow boundary of the computational domain. A nonslip boundary condition is applied to the surface of the airfoil where the density is extrapolated from the adjacent nodes, and the pressure is defined from the equilibrium condition of the momentum normal to the wall. A periodic boundary condition is used in the spanwise direction.

G. Treatments of Transition

For the LES of the flow around an airfoil near the stall condition presented in Ref. 2, turbulent transition is successfully resolved directly with enormous grid points. On the other hand, turbulent transition that occurs inside the boundary layer is not directly resolved in the present LES/RANS hybrid methodology because the turbulence model is used near the solid surface. Because turbulent transition occurs somewhere around the NACA 64A006 airfoil under the present flow conditions, transition models should be introduced to the current turbulence model in the LES/RANS hybrid methodology. In this study, transition to turbulence is simulated by setting the turbulent eddy viscosity $\mu_t = 0$ everywhere upstream of the transition point. The line of transition is specified at $0.002c$ from the leading edge for both the computations using a compact difference scheme and a conventional upwind scheme. The choice of the transition location at $0.002c$ was based on the RANS previous study in Ref. 33. In Ref. 33, several transition locations were chosen manually, and the result with transition at $0.002c$ showed better (but not satisfactory) prediction. Fixed transition location would be good enough when the location is known. From an engineering viewpoint as a design tool, however, it may be desired to determine transition points by the computation itself. Thus, as a simple prediction method, the transition model implemented in the original BL turbulence model[19] is also considered for the computations using a compact difference scheme. In the numerical transition method, the effect of transition to turbulence is simulated by setting turbulent eddy viscosity $\mu_t = 0$ everywhere in a profile of a wall-normal direction, where the maximum tentatively computed value of μ_t is less than a specified value C_{MUTM}; $\mu_t = 0$ if $(\mu_t)_{\max \text{ in profile}} < C_{\text{MUTM}} = 14$. All of the computational cases are listed in Table 1.

III. Numerical Results

A. Flow Conditions

The flow conditions are based on the experiments for the airfoil of McCullough and Gault.[11,12] According to the experiments, freestream Mach number is set to be $M_\infty = 0.17$, and Reynolds number is $(Re = u^*_\infty c^*/\nu^* =)\ 5.8 \times 10^6$. The angle of attack ranges from 4.0 deg for an attached flow through 11.0 deg for a massively separated flow after stall.

B. Computational Setup

1. Grid Sensitivity Study

The computational grid around the NACA 64A006 airfoil used in this study is topologically a C-type, and the x, y, and z directions correspond to the streamwise, spanwise, and wall-normal directions, as shown in Fig. 3. Three computational grids are used to evaluate the simulation sensitivity to the different spatial resolutions. All of the designed grids have a computational domain that extends to $20c$ and $0.5c$ for the outer and spanwise boundaries, respectively. The number of the grid points is listed in Table 2.

Figure 4 shows the time-averaged pressure distributions over the airfoil on each grid at 5.5-deg angle of attack. The laminar separation bubble that appears on the suction surface is a well-known flow characteristics of a NACA 64A006 airfoil under the flow conditions. All of the computations are carried out using the LES/RANS hybrid methodology with a sixth-order compact scheme, and the line of transition is specified at $0.002c$ from the leading edge. Because the results with the baseline grid and fine grid are reasonably approached to the experiment with increasing mesh resolution, the spatial resolution of the baseline grid is considered to have an adequate mesh resolution to simulate thin-airfoil stall phenomena with the current hybrid method. However, a fine grid is used in the present study to improve the spatial resolution and reveal detailed flow mechanisms.

Table 2 Grid characteristics

Grid	Suction side	Pressure side	Wake	Spanwise	Normal to wall	N_{total}
Coarse	126	126	22	26	79	1.18×10^6
Baseline	190	126	22	51	95	1.73×10^6
Fine	252	126	22	51	119	2.54×10^6

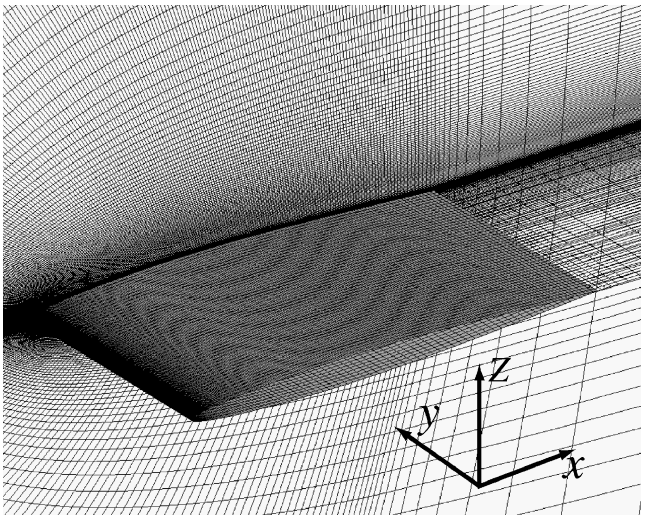

Fig. 3 Computational grid: fine grid, 419 × 51 × 119.

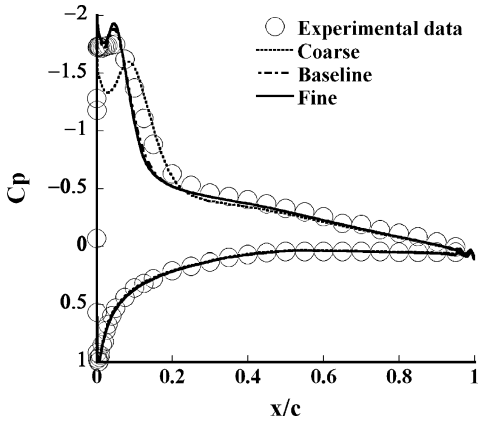

Fig. 4 Time-averaged pressure coefficient distributions over airfoil on three different mesh resolutions, $\alpha = 5.5$ deg.

The average mesh resolution of the fine grid on the upper surface of the wing is $(\Delta x^+, \Delta y^+, \Delta z^+) = (537, 1469, 1.8)$ at $\alpha = 9$ deg (close to stall). The mesh resolution is relatively coarse compared to the LES of the flow around an airfoil near stall.[2–4] Because the near-wall turbulence is fully modeled, the LES/RANS hybrid methodology properly resolves the wall shear stress even with such a relatively coarse mesh resolution, which contributes to the reduction of the computational costs compared to pure LES.

2. Temporal Accuracy

For LES computations, unsteady motion needs to be resolved both in time and space. Therefore, the local Courant–Friedrichs–Lewy (CFL) number must be kept at a magnitude of order unity (see Ref. 34) or an appropriate number of inner iterations must be used for the implicit time-integration method.

To determine the suitable number of inner iterations, the effect of four different numbers of inner iterations, 0, 3, 5, and 10, is investigated. The computational time step is fixed as $\Delta t = \Delta t^* \times u^*_\infty / c^* = 3.4 \times 10^{-4}$. The local CFL number at the interface of the RANS and LES regions is about 3.3 for the time step. The angle of attack is set to be 9 deg, where maximum lift is obtained and aerodynamic coefficients are considered to be highly influenced by the unsteady vortex shedding from the leading edge.

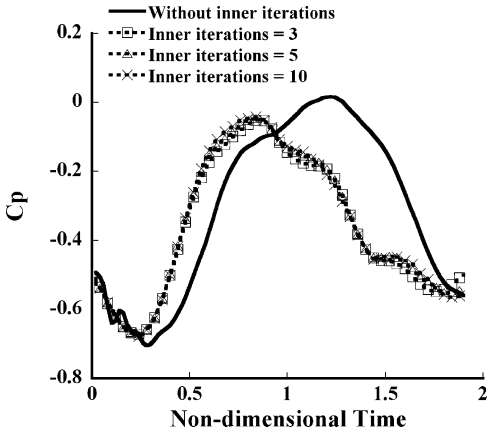

Fig. 5 Time histories of pressure coefficient at position 0.4*c* from leading edge and center in the spanwise direction, $\alpha = 9$ deg.

Time histories of the pressure coefficient at the position of $0.4c$ from the leading edge and the center in the spanwise direction are shown in Fig. 5. Unsteady behavior of the pressure on the airfoil caused by the unsteady vortices shedding from the leading edge is clearly shown, and the computation without inner iterations results in the time delay of the pressure variation. For the number of inner iterations of 3, 5, and 10, there is no time delay, and the features of the pressure variations are almost the same for all of the cases. From the results, the number of inner iterations of three with $\Delta t = 3.4 \times 10^{-4}$ is considered to be sufficient to maintain the temporal accuracy and evaluate the stall features. In this study, the number of inner iterations is set as three with $\Delta t = 3.4 \times 10^{-4}$.

3. Data Processing

The time step $\Delta t = 3.4 \times 10^{-4}$ in nondimensional time corresponds to $\Delta t = 8.96 \times 10^{-6}$ s in dimensional time based on the chord length ($c = 1.524$ m) in the experiment.[11,12] Time-averaged data are created by averaging about 26,000 steps of unsteady flows, which is about 0.233 s as physical time.

C. Results

Because a separation phenomenon is very sensitive to the boundary-layer profile, the boundary layer must be computed correctly. Computed time-averaged boundary-layer velocity profiles on the suction surface ($x/c = 0.1$, 0.2, 0.3, and 0.5) at a 4.0-deg angle of attack are compared with the experiment[12] in Fig. 6, where the boundary-layer velocity profiles are computed from the static and total pressures according to the following relationship:

$$\frac{u}{u_{\text{BL}}} = \sqrt{\frac{p_t - p}{p_{t\infty} - p_{\text{BL}}}} \tag{12}$$

The names of the cases in Fig. 6 indicate the numerical scheme and the transition model that are used in the computation, as shown in Table 1. The growth and shape of the boundary layer highly depend on the mesh resolution in LES, and the required mesh resolution is enormous, as shown in Ref. 3. The flow is fully attached at a 4.0-deg angle of attack, and so the hybrid method is operating almost in RANS mode. The present LES/RANS hybrid methodology can successfully predict the growth and shape of the boundary-layer profiles reasonably well at all of the locations because of the nature of the method under comparatively coarse mesh resolution compared with the required mesh resolution for pure LES. The reduction of

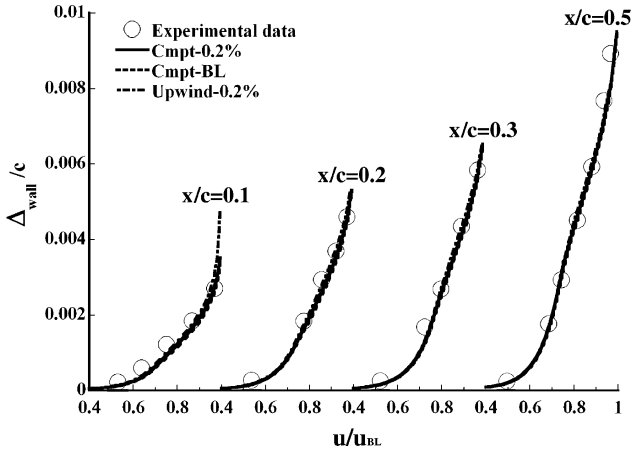

Fig. 6 Boundary-layer velocity profiles developed along the suction surface ($x/c = 0.1$, 0.2, 0.3, and 0.5) at 4-deg angle of attack.

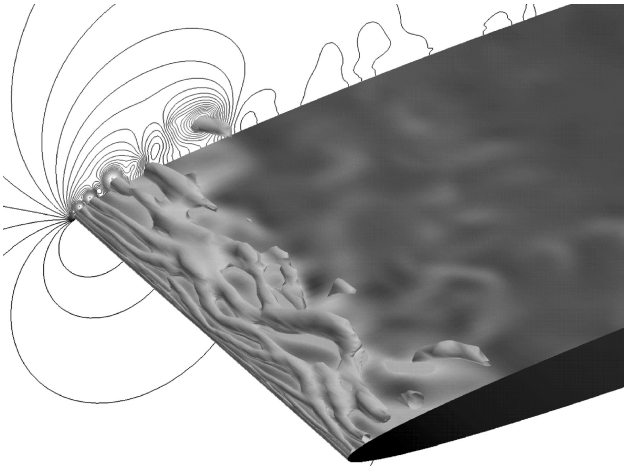

Fig. 7 Instantaneous pressure distribution over airfoil surface and total pressure isosurface of $p_t/p_{t\infty} = 0.96$ at 5.5-deg angle of attack: Cmpt-0.2%.

computational cost compared to LES is clear, as is presented in Sec. III.B.1.

It is well known that the flow characteristics of a NACA 64A006 airfoil under the present flow condition are classified into three types: attached flow at relatively low angle of attack, laminar bubble flow at 5.0-deg angle of attack through the stall angle, and fully separated flow after the stall angle. The mechanism of the laminar bubble is often explained in literatures as follows. Laminar flow separation occurs near the leading edge, and turbulent reattachment occurs somewhere downstream, which causes the formation of the laminar bubble. The appearance of the bubble on the suction surface is the main mechanism of the thin-airfoil stall phenomena. Therefore, it is important to resolve the bubble correctly for the prediction of the stall feature of this airfoil.

The existence of the laminar small bubble near the leading edge is known to be the flow feature of a NACA 64A006 airfoil at 5.5-deg angle of attack. Figures 7 and 8 show the instantaneous pressure distributions over the airfoil surface and the total pressure isosurface of $p_t/p_{t\infty} = 0.96$ obtained by the compact difference scheme (Cmpt-0.2%) and the conventional upwind scheme (Upwind-0.2%), respectively. Separation from the leading edge and unsteady vortices shedding caused by the instability of the shear layer are clearly observed in both of the results. However, there are differences in the position and concentration of the vortices. The result obtained by the compact difference scheme properly resolves small vortices shedding immediately after the laminar separation and uneven pressure distribution patterns resulting from the existence of a three-dimensional vortices structure, as shown in Fig. 7. In contrast, the small vortices shedding are not well resolved in the result obtained by the conventional

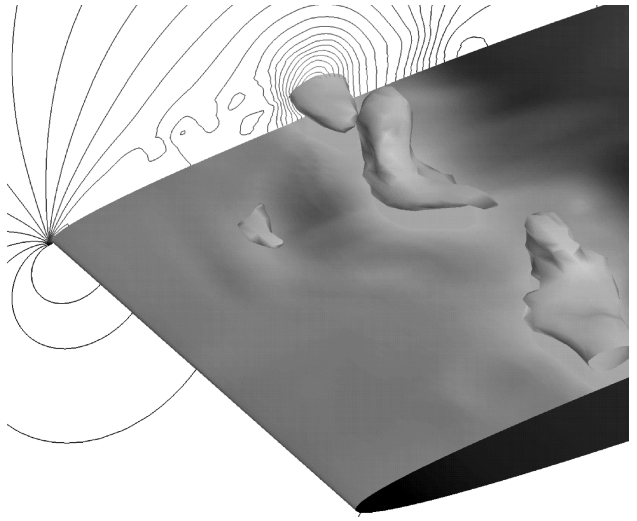

Fig. 8 Instantaneous pressure distribution over airfoil surface and total pressure isosurface of $p_t/p_{t\infty} = 0.96$ at 5.5-deg angle of attack: Upwind-0.2%.

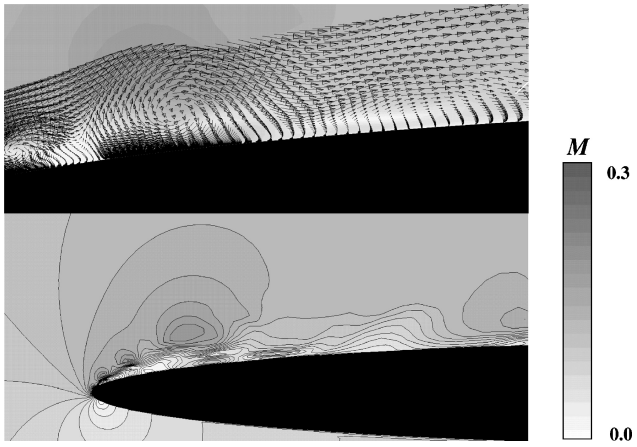

Fig. 9 Instantaneous Mach number distribution and velocity vectors near leading edge at 5.5-deg angle of attack: Cmpt-0.2%.

upwind scheme (Upwind-0.2%), as shown in Fig. 8. Relatively dissipated vortices are generated from about 20% chord length. The conventional upwind scheme may introduce excessive dissipation that stabilizes the shear layer and delays the location of the vortices shedding under the present mesh resolution, whereas the compact difference scheme evaluates the shear layer and vortices without excessive numerical dissipation.

Instantaneous and time-averaged Mach number distributions and velocity vectors near the leading edge obtained by the Cmpt-0.2% case are shown in Figs. 9 and 10. Unsteady flow features induced by the small vortices shedding from the leading edge are observed in the separated regions, as shown in Fig. 9. In the instantaneous flowfields shown in Fig. 9, the existence of the typical laminar small bubble is not clearly observed. On the other hand, the time-averaged flowfield presented in Fig. 10 clearly shows the laminar separation with turbulent reattachment a short distance behind the leading edge where the laminar small bubble is formed. Such a flowfield is also observed in the experiments by Fitzgerald and Mueller[35] using laser Doppler velocimetry measurement. From the computational results shown in Figs. 7, 9, and 10, the typical laminar small bubble near the leading edge at relatively low angles of attack, which is often observed in the experiment and which exists stationary on the suction surface, is considered to be the phenomenon observed as a time-averaged flowfield of the unsteady small vortices shedding for a certain time length. The computational results suggest that the stationary bubble dose not exist practically, but that the unsteady small vortices shedding do exist. Recent improvement of the time resolution in an

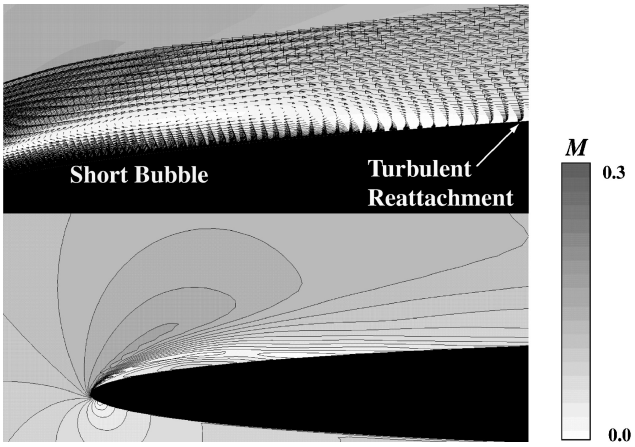

Fig. 10 Time-averaged Mach number distribution and velocity vectors near leading edge at 5.5-deg angle of attack: Cmpt-0.2%.

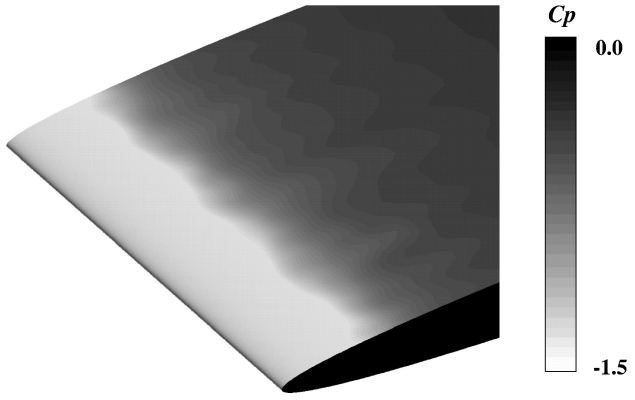

Fig. 11 Time-averaged pressure distribution over airfoil surface at 5.5-deg angle of attack: Cmpt-0.2%.

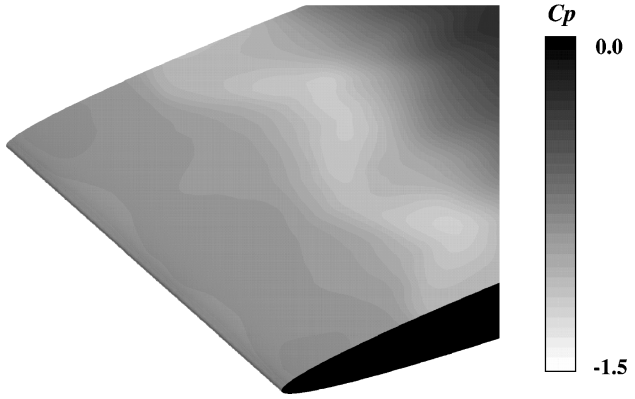

Fig. 12 Time-averaged pressure distribution over airfoil surface at 5.5-deg angle of attack: Upwind-0.2%.

experiment may help to resolve the mechanism of the formation of the bubble.

Time-averaged static pressure distributions over the airfoil surface computed by the Cmpt-0.2% and Upwind-0.2% cases are shown in Figs. 11 and 12, respectively. Three-dimensional flow structures are somewhat lost, and the averaged flowfield is more two dimensional. Regions of low pressure, indicative of the laminar separation bubble, are observed in both the results. However, there is a difference in the low-pressure regions between Figs. 11 and 12. Figure 13 shows the computed time-averaged pressure coefficient distributions over the airfoil compared with the experimental data. The compact difference scheme successfully captures the negative pressure peak caused by the bubble near the leading edge, and both the strength and the position agree well with the experiment. The result with the simple transition method in the BL turbulence model with

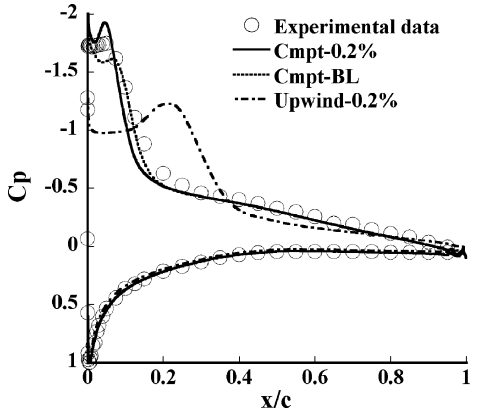

Fig. 13 Time-averaged pressure coefficient distributions over airfoil at 5.5-deg angle of attack.

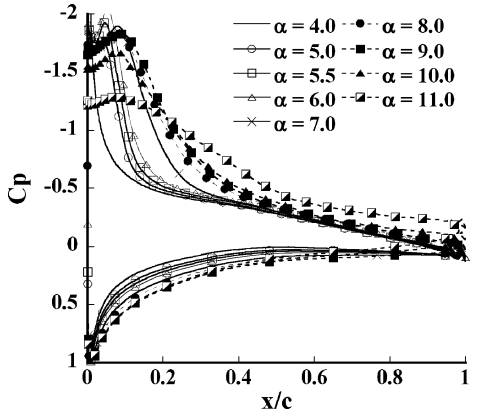

Fig. 14 Time-averaged pressure coefficient distributions over airfoil at angle of attack range 4.0–11.0 deg: Cmpt-0.2%.

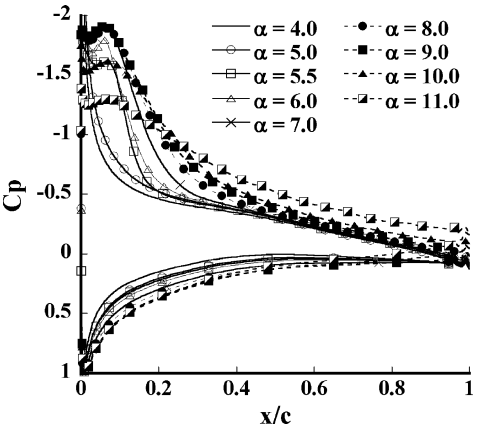

Fig. 15 Time-averaged pressure coefficient distributions over airfoil at angle of attack range 4.0–11.0 deg: Cmpt-BL.

the compact difference scheme also successfully predicts the pressure distribution. In contrast, the conventional upwind scheme fails to capture the formation of small bubble near the leading edge, and extensive negative pressure is observed at $0.2c$ behind the leading edge. The discrepancy from the experiment comes from the numerically dissipated shear layer and vortices shedding as shown in Fig. 8.

Figures 14–16 show the time-averaged pressure coefficient distributions over the airfoil surface at different angles of attack obtained by Cmpt-0.2%, Cmpt-BL, and Upwind-0.2%, respectively. The results obtained by the compact difference scheme as shown in Figs. 14 and 15 successfully capture the suction peak near the leading edge caused by the laminar small bubble at relatively low angles of attack. Growth of the length of the laminar bubble and a gradually collapsed suction peak are well resolved, where the reattachment point moves

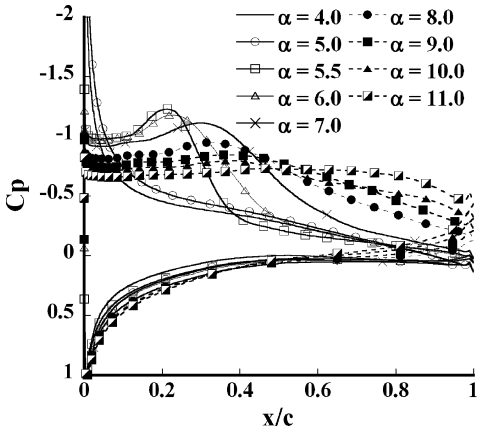

Fig. 16 Time-averaged pressure coefficient distributions over airfoil at angle of attack range 4.0–11.0 deg: Upwind-0.2%.

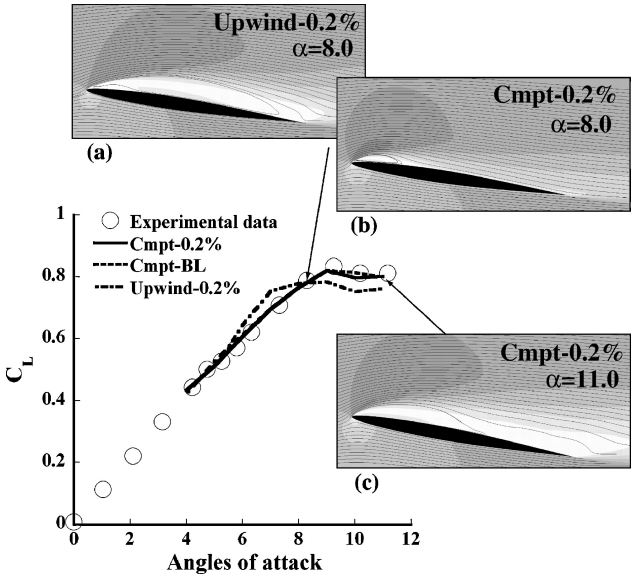

Fig. 17 Lift coefficient vs angles of attack and key flowfields over the airfoil at 8.0- and 11.0-deg angles of attack.

toward the trailing edge with the angle of attack increase. The growth of the bubble is also observed in the experiment with increasing angles of attack. The current treatment of transition adopted in the BL turbulence model works well together with the hybrid method to capture the typical laminar small bubble at relatively low angles of attack and its growth with increasing angles of attack. In contrast, Fig. 16 shows that the Upwind-0.2% computations cannot capture the laminar small bubble and its growth with increasing angles of attack. The suction pressure peak is not resolved at all, and relatively flat pressure distributions over the airfoil are observed. This is considered to be due to the lack of present mesh resolution for the LES with a conventional upwind scheme, as discussed earlier.

The time-averaged lift characteristic is important from an engineering viewpoint. Figure 17 shows the computed lift characteristics compared with the experimental data of McCullough and Gault.[11] Time-averaged Mach number distributions and streamlines of the key flowfields are also included in Figs. 17a–17c. The experimental data are corrected for the consideration of the tunnel-wall constraint and the effects of compressibility. The results obtained by the compact difference scheme show that proper estimations of the slope of the lift curves, the maximum lift, and the stall angle are successfully achieved. Quantitative prediction of the stall feature seems to be satisfactorily captured even after the stall angle, where the massively separated unsteady flows induced by the vortices shedding from the leading edge are dominant. The LES/RANS hybrid methodology with the simple BL transition method works extremely well with the flows around the NACA 64A006 airfoil to predict the thin-airfoil stall characteristics, where transition points should be determined by the computation itself. At relatively low angles of attack, the bubble gradually grows rearward where the suction pressure peak is maintained at almost the same level. Therefore, the lift increases linearly. The thin-airfoil stall occurs when the bubble progressively grows rearward with a gradually collapsed suction peak at high angles of attack, as shown in Figs. 14, 15, 17b, and 17c. According to the gradually collapsed negative pressure, a sudden loss of lift at the stall does not occur. On the other hand, the conventional upwind scheme slightly overpredicts the lift at the angles of attack from 5.5 to 7 deg. The flow is fully separated without any reattachment on the airfoil surface at an 8-deg angle of attack, as shown in Fig. 17a, whereas the bubble near the leading edge is well resolved by the computation with the compact difference scheme, as shown in Fig. 17b. Relatively flat pressure distribution along the entire upper surface induced by the fully separated flowfield is observed in Fig. 16. In contrast with the results obtained by the Cmpt-0.2% and Cmpt-BL, a further increase in lift cannot be expected anymore. At angles of attack greater than 7 deg, therefore, the slope of the lift curve is reduced and the peak of the curve is rounded. Compared with the experiments, the predicted stall angle is smaller by 2 deg, and the obtained maximum lift is slightly underpredicted. The reason for this discrepancy is that the laminar small bubble and its growth with the collapsed suction pressure is not well resolved, and the flows are fully separated without any reattachment at a relatively low angle of attack under the current mesh resolution.

The compact difference scheme provides much more reliable results than does the conventional upwind scheme under the current mesh resolution. Simulation using a conventional upwind scheme fails to predict the flow characteristics. With much a larger number of grid points, such simulation would capture the laminar small bubble at relatively low angles of attack and its growth with increasing angles of attack, but that would require a much higher computational cost. One important issue here is that the simulation with the LES/RANS hybrid methodology, coupled with the high-resolution compact difference scheme, allows us to simulate the flowfield within the restricted number of grid points (about 3 million) and available personal-computer class computer memory. From the successful prediction obtained by the LES[3] in LESFOIL project, required mesh resolution near the solid surface is $(\Delta x^+, \Delta y^+, \Delta z^+) = (60, 25, 2)$. When the required mesh resolution is considered, the capability of the present LES/RANS hybrid method with the compact difference scheme is significant. The computational cost may be reduced roughly 500 times lower than that of pure LES to compute the same size domain. The other important issue is that the thin-airfoil stall characteristics are well simulated using the LES/RANS hybrid methodology.

IV. Conclusions

A thin-airfoil stall feature of a NACA 64A006 airfoil is computationally investigated using LES/RANS hybrid methodology with the high-order compact difference scheme at several flow conditions: subsonic flow of $M_\infty = 0.17$, high Reynolds number of $Re = 5.8 \times 10^6$, and angle of attack range 4.0–11.0 deg. The thin-airfoil stall phenomena are characterized by laminar flow separation at the leading edge and turbulent reattachment, where the reattachment point gradually moves rearward with increasing angles of attack.

Thin-airfoil stalling aerodynamic characteristics, which are of primary interest from an engineering viewpoint, were successfully predicted using the LES/RANS hybrid methodology with a high-order compact difference scheme with a reasonable computational cost, whereas LES alone may not be suitable for this kind of parametric (various angles of attack) study because of its high computational cost. The RANS simulations with any turbulence model have never been successful as far the authors know. The time-averaged pressure distribution over the airfoil surface showed that the laminar small bubble at relatively low angles of attack and its growth with increasing angles of attack were successfully captured. For the prediction of thin-airfoil stall phenomena, it is necessary to resolve properly the laminar small bubble near the leading edge and the growth of the bubble where suction pressure peak is collapsed with

increasing angles of attack. The growth and shape of the boundary-layer profiles over the suction surface were successfully predicted even under a relatively coarse mesh resolution compared with the required mesh resolution for pure LES. The vortices shedding from the leading edge were properly resolved without excessive dissipation under the current mesh resolution with the high-order compact difference scheme. From the instantaneous and time-averaged flows, it has been confirmed that the typical laminar small bubble near the leading edge observed in the experiments is a phenomenon when the unsteady vortices shedding from the leading edge are averaged for a certain time length.

In the investigation of different schemes under the current mesh resolution, the conventional upwind scheme failed to resolve properly the small vortices shedding from the leading edge in the instantaneous flowfield and the laminar small bubble and growth of the bubble with increasing angles of attack in the time-averaged flowfields, but would capture the thin-airfoil stall phenomena if a much larger number of grid points were used. One important issue here is that the LES/RANS hybrid methodology with the high-order compact difference scheme provided extremely high-fidelity results for the complicated and separated flowfields associated with a NACA 64A006 airfoil near stall within the restricted number of grid points (about 3 million) and available personal-computer-class computer memory.

Regarding the treatment of transition, the numerical transition method implemented in the original turbulence model by Baldwin and Lomax that detects the transition point automatically from the simulation itself worked well with the hybrid method for the flows around the NACA 64A006 airfoil. Laminar small bubble at relatively low angles of attack and its growth with increasing angles of attack and the aerodynamic characteristics were successfully predicted with the simple automatic detection method. In the present LES/RANS hybrid methodology, transition near the wall region must be computed by RANS. Therefore, the hybrid method with the simple transition method is considered to be an effective prediction tool for flows where RANS can predict the transition reasonably well; the present flow and the flow past a circular cylinder[7] where leading-edge separation determines transition (bypass transition) are such cases.

In total, the results illustrated the possibility of the LES/RANS hybrid methodology for the prediction of massively separated high Reynolds number flows with laminar separation and turbulent reattachment within a more practical computational cost than that of pure LES approaches.

Acknowledgment

This work was financed by the Japan Society for the Promotion of Science (Project 16-10764). The first author appreciates their support.

References

[1]Takaki, R., Yamamoto, K., Enomoto, S., Yamazaki, H., Yamane, T., and Iwamiya, T., "Numerical Simulation of 2D Airfoil Stall by UPACS-CFD Workshop on 2D Airfoil Stall Predict," *Proceedings of the Aerospace Numerical Simulation Symposium 2000*, National Aeronautical Lab., NAL SP-46, Tokyo, 2000, pp. 163–168.

[2]Mellen, P. C., Fröhlich, J., and Rodi, W., "Lessons from LESFOIL Project on Large-Eddy Simulation of Flow Around an Airfoil," *AIAA Journal*, Vol. 41, No. 4, 2003, pp. 573–581.

[3]Mary, I., and Sagaut, P., "Large Eddy Simulation of Flow Around an Airfoil Near Stall," *AIAA Journal*, Vol. 40, No. 6, 2002, pp. 1139–1145.

[4]Dahlström, S., and Davidson, L., "Large Eddy Simulation of the Flow Around an Airfoil," AIAA Paper 2001-0425, Jan. 2001.

[5]Georgiadis, N. J., Alexander, J. I. D., and Reshotko, E., "Hybrid Reynolds-Averaged Navier–Stokes/Large-Eddy Simulations of Supersonic Turbulent Mixing," *AIAA Journal*, Vol. 41, No. 2, 2003, pp. 218–229.

[6]Kawai, S., and Fujii, K., "Computational Study of a Supersonic Base Flow Using LES/RANS Hybrid Methodology," AIAA Paper 2004-0068, Jan. 2004.

[7]Spalart, P. R., Jou, W-H., Strelets, M., and Allmaras, S. R., "Comments on the Feasibility of LES for Wings and on the Hybrid RANS/LES Approach," *Advances in DNS/LES, 1st AFOSR International Conference on DNS/LES*, Greyden Press, Columbus, OH, 1997, pp. 137–147.

[8]Spalart, P. R., and Allmaras, S. R., "A One-Equation Turbulence Model for Aerodynamic Flows," AIAA Paper 92-0439, Jan. 1992.

[9]Travin, A., Shur, M., Strelets, M., and Spalart, P. R., "Detached-Eddy Simulations Past a Circular Cylinder," *Flow, Turbulence and Combustion*, Vol. 63, No. 1–4, 1999, pp. 293–313.

[10]Lele, K. S., "Compact Finite Difference Schemes with Spectral-like Resolution," *Journal of Computational Physics*, Vol. 103, No. 1, 1992, pp. 16–42.

[11]McCullough, G. B., and Gault, D. E., "Examples of Three Representative Types of Airfoil-Section Stall at Low Speed," NACA TN2502, Sept. 1951.

[12]McCullough, G. B., and Gault, D. E., "Boundary-Layer and Stalling Characteristics of the NACA64A006 Airfoil Section," NACA TN1923, Aug. 1949.

[13]Smagorinsky, J., "General Circulation Experiments with the Primitive Equations, Part1: The Basic Experiment," *Monthly Weather Review*, Vol. 91, No. 3, 1963, pp. 99–152.

[14]Yoshizawa, A., "Statistical Theory for Compressible Turbulent Shear Flows, with the Application to Subgrid Modeling," *Physics of Fluids*, Vol. 29, No. 7, 1986, pp. 2152–2164.

[15]Moin, P., Squires, K., Cabot, W., and Lee, S., "A Dynamic Subgrid-Scale Model for Compressible Turbulence and Scalar Transport," *Physics of Fluids A*, Vol. 3, No. 11, 1991, pp. 2746–2757.

[16]Vreman, A. W., "Direct and Large-Eddy Simulation of the Compressible Turbulent Mixing Layer," Ph. D. Dissertation, Univ. of Twente, Twente, The Netherlands, Dec. 1995.

[17]Vreman, B., Geurts, B., and Kuerten, H., *Subgrid-Modeling in LES of Compressible Flow, Direct and Large-Eddy Simulation 1*, Kluwer Academic, Dordrecht, The Netherlands, 1994, pp. 133–144.

[18]Vreman, B., Geurts, B., and Kuerten, H., "Realizability Conditions for the Turbulent Stress Tensor in Large-Eddy Simulation," *Journal of Fluid Mechanics*, Vol. 278, 1994, pp. 351–362.

[19]Baldwin, B., and Lomax, H., "Thin Layer Approximation and Algebraic Model for Separated Turbulent Flows," AIAA Paper 78-257, Jan. 1978.

[20]Lund, S. T., Wu, X., and Squires, D. K., "Generation of Turbulent Inflow Data for Spatially-Developing Boundary Layer Simulations," *Journal of Computational Physics*, Vol. 140, No. 2, 1998, pp. 223–258.

[21]Spalart, P. R., "Young-Person's Guide to Detached-Eddy Simulation Grids," NASA CR-2001-211032, July 2001.

[22]Erlebacher, G., Hussaini, Y. M., Speziale, G. C., and Zang, A. T., "Toward the Large-Eddy Simulation of Compressible Turbulent Flows," NASA CR-187460, Oct. 1990.

[23]Rogallo, R. S., and Moin, P., "Numerical Simulation of Turbulent Flows," *Annual Review of Fluid Mechanics*, Vol. 17, 1984, pp. 99–137.

[24]Gordnier, E. R., and Visbal, R. M., "Higher-Order Compact Difference Scheme Applied to Simulation of a Low Sweep Delta Wing Flow," AIAA Paper 2003-0620, Jan. 2003.

[25]Arasawa, T., Fujii, K., and Miyaji, K., "High-Order Compact Difference Scheme Applied to Double-Wing Vortical Flows," *Journal of Aircraft*, Vol. 41, No. 4, 2004, pp. 953–957.

[26]Morgan, E. P., and Visbal, R. M., "Large-Eddy Simulation of Airfoil Flows," AIAA Paper 2003-0777, Jan. 2003.

[27]Koutsavdis, K. E., Blaisdell, A. G., and Lyrintzis, S. A., "A Numerical Investigation of Two-Dimensional Jets Using Spatial Filtering," AIAA Paper 99-27942, Jan. 1999.

[28]Gaitonde, V. D., and Visbal, R. M., "Further Development of a Navier–Stokes Solution Procedure Based on Higher-Order Formulas," AIAA Paper 99-0557, Jan. 1999.

[29]Shima, E., and Jounouchi, T., "Role of CFD in Aeronautical Engineering (No.14)-AUSM Type Upwind Schemes," *Proceedings of the 14th NAL Symposium on Aircraft Computational Aerodynamics*, National Aeronautical Lab., Tokyo, 1997, pp. 7–12.

[30]Liou, M. S., and Steffen, C. J., Jr., "A New Flux Splitting Scheme," *Journal of Computational Physics*, Vol. 107, No. 1, 1993, pp. 23–39.

[31]van Leer, B., "Towards the Ultimate Conservative Difference Scheme 5. A Second-Order Sequel to Godunov's Method," *Journal of Computational Physics*, Vol. 32, No. 1, 1979, pp. 101–136.

[32]Yoon, S., and Jameson, A., "Lower–Upper Symmetric-Gauss–Seidel Method for the Euler and Navier–Stokes Equations," *AIAA Journal*, Vol. 26, No. 9, 1988, pp. 1025–1026.

[33]Hasuike, T., Oyama, A., Nakahashi, K., and Obayashi, S., "CFD Stall Predictions of 2D Airfoils," *Journal of the Japan Society for Aeronautical and Space Sciences*, Vol. 50, No. 577, 2002, pp. 56–63.

[34]Choi, H., and Moin, P., "Effects of the Computational Time Step on Numerical Solutions of Turbulent Flow," *Journal of Computational Physics*, Vol. 113, No. 1, 1994, pp. 1–4.

[35]Fitzgerald, J. E., and Mueller, J. T., "Measurements in Separation Bubble on an Airfoil Using Laser Velocimetry," *AIAA Journal*, Vol. 28, No. 4, 1990, pp. 584–592.

D. Gaitonde
Associate Editor